Earth and Planetary Science Letters 604 (2023) 118011

Contents lists available at ScienceDirect

Earth and Planetary Science Letters

journal homepage: www.elsevier.com/locate/epsl

Wavefield distortion imaging of Earth's deep mantle

Sebastian Rost [a,*], Daniel A. Frost [b,1], Andy Nowacki [a], Laura Cobden [c]

[a] School of Earth and Environment, University of Leeds, Woodhouse Lane, Leeds, LS2 9JT, United Kingdom
[b] Department of Earth & Planetary Science, University of California, Berkeley, 307 McCone Hall, Berkeley, CA 94720-4767, USA
[c] Department of Earth Sciences, Utrecht University, Princetonlaan 8a, 3584 CB Utrecht, The Netherlands

ARTICLE INFO

Article history:
Received 17 August 2022
Received in revised form 3 January 2023
Accepted 10 January 2023
Available online 26 January 2023
Editor: H. Thybo

Keywords:
array seismology
lower mantle structure
seismic velocity
mantle plume
subduction

ABSTRACT

The seismic wavefield, as recorded at the surface, carries information about the seismic source and Earth's structure along the seismic path, essential for the understanding of the interior of our planet. For 40 years seismic tomography studies have resolved the 3D seismic velocity structure in growing detail using seismic traveltimes and waveforms. These studies have been driving our understanding of the dynamics and evolution of the planet, but are limited in their spatial resolution to imaging scales of a few 100 s to 1000 km due to the constraints of the tomographic inversion. Detailed studies of seismic waveforms can resolve finer scale structure but are often reliant on serendipitous source-receiver combinations and provide very uneven coverage of the planet. Therefore, we often lack an understanding of the fine scale structure of the Earth that is important to understand structures and processes such as mantle plumes or details of slab recycling. Here we show evidence that we can exploit slowness vector deviations of the seismic wavefield to extend our knowledge of Earth structure to smaller scales using large datasets. Analysing seismic array data, we show strong and measurable focussing and defocussing effects of the teleseismic P and P_{diff} wavefield sampling the deep Earth. We compare the P-wave results to additional S and S_{diff} data and find good agreement between both wavetypes. We can link the wavefield deviations to strong velocity variations assuming sharp boundaries are sampled along the path in the deep mantle. The dataset samples the Pacific and Gulf of Mexico well and shows strong horizontal incidence (backazimuth) deviations in the Pacific (up to 14° westwards) and beneath the Gulf of Mexico (up to 5 to 8° east- and west-ward). The backazimuth deviations are also reflected in slowness deviations in the range of $\pm$ 0.8 s/° relating to velocity variations in the range of $\pm$ 9 km/s. Using 3D raytracing we are able to forward model the detected backazimuth variations of the P and P_{diff} dataset. The high frequencies of the P-waves, density of the ray-paths, and low computational cost of our forward calculation allow us to construct a higher resolution and more detailed model of velocity anomalies under Hawaii than was possible with previous methods. The best-fitting velocity model for the Pacific contains two low-velocity regions located at N25°/W155° and N25°/W165° beneath the tip of the Hawaii Emperor chain. The Pacific anomalies have diameters (D) of 6° and 2° with velocity reductions (dV_P) of 8% and 4% with heights (H) above the CMB of 70 km and at least 200 km, respectively. We also detect a fast region of 3% velocity increase in the North Pacific rising at least 300 km above the CMB with a diameter of 12° at N60°/W175°. Beneath the Gulf of Mexico we find ambiguous results with either a slow region (N25°/W85°, H = 200 km, dV_P=-3%, D = 2°) or a fast region (N15°/W75°, H = 200 km, dV_P = 3%, D = 4°) able to explain the data. We thus show that the directivity information of the seismic wavefield - largely underexploited - can be used to resolve the fine scale velocity structure of the Earth's interior with great accuracy and can deliver additional insight into deep Earth dynamics.

1. Introduction

Tomographic models of the Earth's lowermost mantle are dominated by two continent-sized, nearly equatorial and antipodal regions of reduced seismic velocities (e.g. Ritsema et al., 2011; French and Romanowicz, 2015) generally called Large Low Velocity Provinces (LLVPs). LLVP locations and shapes are consistent be-

* Corresponding author.
E-mail address: s.rost@leeds.ac.uk (S. Rost).
[1] Now at University of South Carolina.

https://doi.org/10.1016/j.epsl.2023.118011

tween a large number of *S*-wave velocity models (e.g. Lekic et al., 2012) and are separated by areas of higher than average seismic velocities which are commonly interpreted as remnants of subducted slabs in the deep mantle. LLVPs are of unknown origin, and both thermo-chemical (McNamara and Zhong, 2005) and purely thermal (Davies et al., 2012) origins are discussed. LLVPs are characterized by drops in *S*-wave velocity of about 3% (Garnero and McNamara, 2008), sharp boundaries (Ford et al., 2006; Ward et al., 2020), and steep sides (To et al., 2005; Ward et al., 2020). Geodynamic models show that LLVPs change location and configuration dependent on mantle flows in response to subduction. This is supported by the velocity of the interjacent high *S*-wave velocity areas showing increases on the order of 1.5% relative to the average velocity in agreement with existence of subducted slab material in these locales.

Deep seated mantle plumes are proposed as the source for hotspot volcanism and ocean island basalts (Morgan, 1971). The classical thermal mantle plume consists of a large plume head and a narrow conduit transporting material with excess temperatures on the order of 200 K to the surface (Zhong, 2006), although more recent observations indicate broader upwellings connected to intraplate volcanism (e.g. French and Romanowicz, 2015) which is consistent with a thermo-chemical plume model. Plumes might be relatively stationary and anchored to the CMB (Jellinek and Manga, 2002) but can be affected by the background mantle convection (McNamara and Zhong, 2005). Imaging of the traditional narrow plume tails evident in numerical and physical convection studies is difficult due to their diameter generally being well below the resolution of current tomographic models. Nonetheless broader low velocity and inferred hot structures have been detected in recent global tomography models (French and Romanowicz, 2015) potentially casting doubt on the traditional thermal models. The broader upwellings might consist of closely spaced narrower plumes that are not fully resolved by tomography (French and Romanowicz, 2015). But a clear detection of a deep seated plume root is still outstanding. Other seismological methods able to resolve regional seismic structure with higher resolution than global regularized inversions are necessary to image lower mantle plume structures.

Subducted slabs are the major source of compositional heterogeneity in the mantle. While high velocity features in the upper mantle are common in most tomographic models, the velocity anomalies related to slabs seem to disappear around 1000–1400 km depth (Shephard et al., 2017) before apparently representing as high velocity anomalies below ~2500 km depth. The change of the tomographical expression of subducted slabs might be related to changes of tomographic resolution in the mid-mantle, changes of the velocity contrast between the slab and the ambient mantle, changes in subduction flux over time or changes in mantle viscosity inhibiting flow (Shephard et al., 2017). The crustal part of the slab is generally below the resolution of global tomography but crustal remnants have been detected as scatterers of seismic energy in the mid- and lower mantle (Frost et al., 2017) at scales below those resolvable by global tomography. Geochemical analysis of e.g. ocean island basalts provides evidence for the recycling process of crustal components of subducted slabs into the mantle (Hofmann, 1997), however, the detailed physical processes are ill-understood.

Despite current developments in global full waveform tomography the resultant models are not able to resolve the fine scale structure of the mantle due to limitations in frequency. Because of the necessary regularization the resultant models are smooth and are not able to resolve sharp boundaries indicative of strong thermal or compositional heterogeneity. Therefore these models are not able to resolve many of the finer features of mantle structure that will allow us to understand mantle dynamics and evolution. We find that exploiting information beyond traveltimes and waveforms, namely the slowness vector (directivity) of the wavefield allows resolving smaller scale structure and sharp boundaries in the deep Earth.

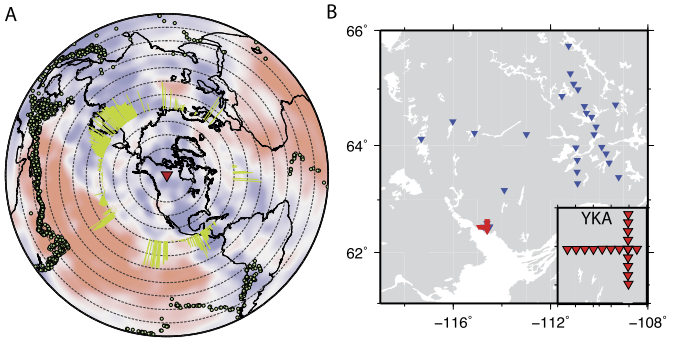

Fig. 1. (A) *P*-wave seismic dataset with sources (circles) recorded at the Yellowknife Array (YKA – inverted triangle). Sampling of the lowermost mantle is indicated by yellow paths (P_{diff}) and circles (*P* turning point location). Distance from YKA is indicated as dashed lines from 20° to 120° distance. Background shows seismic velocities of tomography model by Ritsema et al. (2011) with the structure shown at the core-mantle boundary. (B) Location of POLARIS stations (blue triangles) used for *S*-wave analysis. YKA station configuration is shown in right hand side insert with the YKA location shown as red triangles on map.

To understand important processes such as plume formation and ascent, slab recycling and composition of LLVPs, higher resolution seismic imaging of the lower mantle might be required. Here we present results of wavefield directivity information i.e. deviations of the horizontal and vertical incidence angle of the seismic wavefield, that can be used to resolve smaller scale structure. Deviations of the slowness vector of the seismic wavefield and especially backazimuth (horizontal incidence angle) are able to resolve smaller scale velocity anomalies in the lowermost mantle that might be below the resolution level of tomographic imaging (Stockmann et al., 2019). While exploiting the directivity information directly delivers more insight into mantle structure, including this, currently unused, additional information in tomographic inversions of traveltimes or waveforms might increase our understanding of the structure of the mantle further.

2. Data

We analyse a dataset consisting of 1428 events for the *P*-wave analysis (Fig. 1a) and 225 events for *S*-waves (Fig. 1b). The *P*-wave data are recorded at the medium aperture Yellowknife array (YKA) (Natural Resources Canada (NRCAN Canada), 1975) located in northern Canada (Fig. 1a). Yellowknife consists of up to 19 short-period (dominant period of 1 s), vertical seismometers arranged in a cross shape with 2.5 km interstation spacing. Additionally, up to five broadband, 3-component stations are available. YKA is designed to detect high-frequency seismic *P*-waves and shows high signal coherence and low noise conditions across the array.

Due to the dominantly vertical instrumentation of YKA with lower sensitivity for *S*-waves and its small aperture not well suited for analysis of *S*-waves, we augment the *P*-wave dataset with *S*-wave recordings from up to 29 stations of the POLARIS (Portable Observatories for Lithospheric Analysis and Research Investigating Seismicity - FDSN network code PO) installation in the Canadian Northwest Territories (Fig. 1b).

For the YKA *P*-wave dataset we collect data from events with magnitudes larger than 6.0 from January 2000 to March 2012 in an epicentral distance range between 90° and 115° from the YKA array center, i.e. events just turning up to 150 km above or starting to diffract along the CMB. The POLARIS installation around YKA was temporary, with stations deployed mainly between 2001 and 2007 with a few stations being operative until 2009. The de-

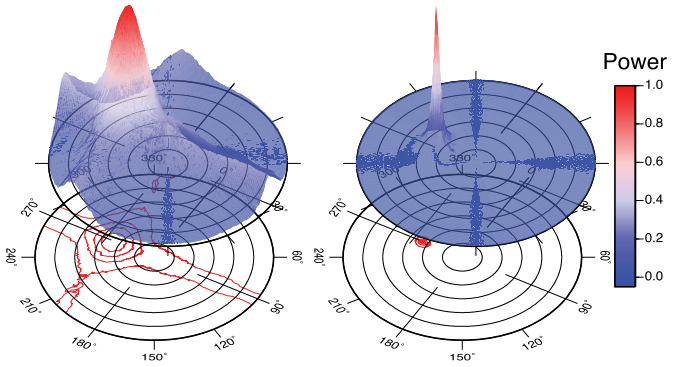

Fig. 2. Improvement of the standard slowness/backazimuth resolution of YKA (left) through the application of the F-statistic (right). Normalised beam-power as a function of beam slowness and backazimuth. Slowness ranges from 0 s/° to 12 s/°.

ployment and decommissioning of stations led to slightly varying station distributions changing the network configuration. To allow good station coverage in the region for our array processing we collect event data from 2002 to 2006 for events with magnitudes larger than 6.0 in the epicentral distance range from 90° to 110° from the network center, again focussing on events turning just above or diffracting for short distances along the CMB.

The data for both datasets cover a wide range of backazimuths. The *P*-wave dataset will allow better sampling of Earth structure and we will use the *S*-wave data to support the *P*-wave observations. The sampling is shown in Fig. 1a) and b) for *P*-waves and *S*-waves, respectively. For the *P*-wave dataset we have especially good sampling across the central Pacific towards the Kamchatka peninsular and Siberia and beneath Central America. The *S*-wave dataset roughly samples the same regions, but contains fewer usable events leading to much sparser sampling. In the Pacific, we partially sample the Large Low Velocity Province (LLVP), especially the region around the Hawaiian hotspot where other studies have detected anomalous structures at the CMB (Kim et al., 2020; Cottaar and Romanowicz, 2012; Jenkins et al., 2021; Li et al., 2022). Beneath Central America and the Gulf of Mexico we sample a region of the lowermost mantle dominated by high seismic velocities in tomography models, which has been linked to subducted slabs reaching the CMB (Hutko et al., 2006) with a low velocity region located towards the East beneath the Gulf of Mexico. Therefore, our dataset potentially allows sampling of different tectonic regimes to resolve the wavefield distortions due to fast and slow velocity regions.

3. Method

To resolve the slowness vector of the incoming wavefield and potential deviations from the expected plane wavefront direction we use array processing. The slowness vector (with the components of vertical and horizontal slowness or slowness and backazimuth) defines the directivity of the incoming wavefront and can be used to locate the earthquake source or, as done here, to characterize the propagation medium. Multiple processing methods have been developed to analyse seismic array data to determine directivity information for source location and characterization. Due to its small aperture, YKA shows limited resolution of the slowness vector for incoming *P*-waves (Fig. 2c), and the array configuration leads to the array response function (ARF) showing strong sidelobes aligned in North-South and East-West direction impeding the exact measurement of the slowness vector and causing varying wavenumber resolution depending on the backazimuth of the incoming wavefront. To increase wavenumber resolution we use the *F*-statistic (Blandford, 1974) which has been shown to improve resolution for small and medium aperture arrays (Selby, 2008). The *F*-statistic (F) is applied to the beam $b(t)$ of the trace to produce the *F*-trace. The *F*-statistic penalizes incoherent energy and arrivals that arrive with different slowness vectors than the coherent energy of the signal. The improved ARF of YKA after applying the *F*-statistics to the beam traces as explained below shows a sharp response approaching a δ-peak with strongly reduced sidelobes (Fig. 2b) allowing more precise determination of the slowness vector.

Let x_c be the signal recorded at the reference station of the array with the individual array stations being characterized by location vectors $\mathbf{r_i}$. The signal recorded consists of the coherent signal $f(t)$ and incoherent noise $n_c(t)$.

$$x_c(t) = f(t) + n_c(t) \tag{1}$$

The signal recorded at a different array element x_i with location vector $\mathbf{r_i}$ is time shifted due to the location difference and the horizontal and vertical incidence angles defined by the slowness vector $\mathbf{u}$

$$x_i(t) = f(t - \mathbf{r_i} \cdot \mathbf{u}) + n_i(t) \tag{2}$$

with the time shifts defining an apparent velocity (V_{app}) of the incident wavefront. The time shifts due to sensor location and incidence direction can be removed to align the coherent signal and suppress the incoherent noise

$$\tilde{x}(t) = x_i(t + \mathbf{r_i} \cdot \mathbf{u}) = f(t) + n_i(t + \mathbf{r_i} \cdot \mathbf{u}) \tag{3}$$

The beam $b(t)$ is now formed as the normalized summation of the time shifted traces $\tilde{x}_i(t)$ from the individual array elements for specific values of backazimuth (θ) and slowness (u)

$$b_{\theta,u}(t) = \frac{1}{N} \sum_{i=1}^{N} \tilde{x}_{i_{\theta,u}}(t) \tag{4}$$

We apply the *F*-trace in form of a grid search over a range of slownesses u and backazimuths θ, defining the vertical and horizontal incidence angle, respectively.

$$F(\theta, u) = (N-1) \frac{N \sum_{t=1}^{M} b_{\theta,u}(t)^2}{\sum_{t=1}^{M} \sum_{i=1}^{N} \left(x_i(t) - b_{\theta,u}(t)\right)^2} \Bigg|_{u=0\ s/^\circ}^{u=12\ s/^\circ} \Bigg|_{\theta=0^\circ}^{\theta=360^\circ} \tag{5}$$

To determine confidence intervals in the measurement of the slowness vector for YKA after applying the *F*-statistic we use a bootstrapping approach (Efron and Tibshirani, 1986). We randomly remove 20% of the array traces while replacing. We perform 200 iterations, which tests show give us stable results of the error estimates. Due to the sharp ARF of the *F*-trace analysis, errors are typically very small (Fig. 3) on the order of less than 1 s/° and 1° for slowness and backazimuth, respectively. Some events show larger errors due to poor signal-to-noise ratios or interfering coherent arrivals. Events with large error estimates are excluded from further analysis.

Before analysis using *F*-beampacking as described in eq. (5) we visually inspect all traces and remove obvious data errors (e.g. outages, spikes, steps). *P*-wave data are filtered between 1.0 and 2.0 Hz and *S*-wave data between 0.05 and 0.1 Hz using a fourth-order bandpass. We perform the *F*-trace stacks for a slowness range from 0 s/° to 12 s/° and all backazimuths (0° to 360°). We choose a time window starting 4 s before the theoretical *P*/*S*-wave arrival according to the 1D Earth model IASP91 (Kennett and Engdahl, 1991) and ending 10 s after this theoretical arrival.

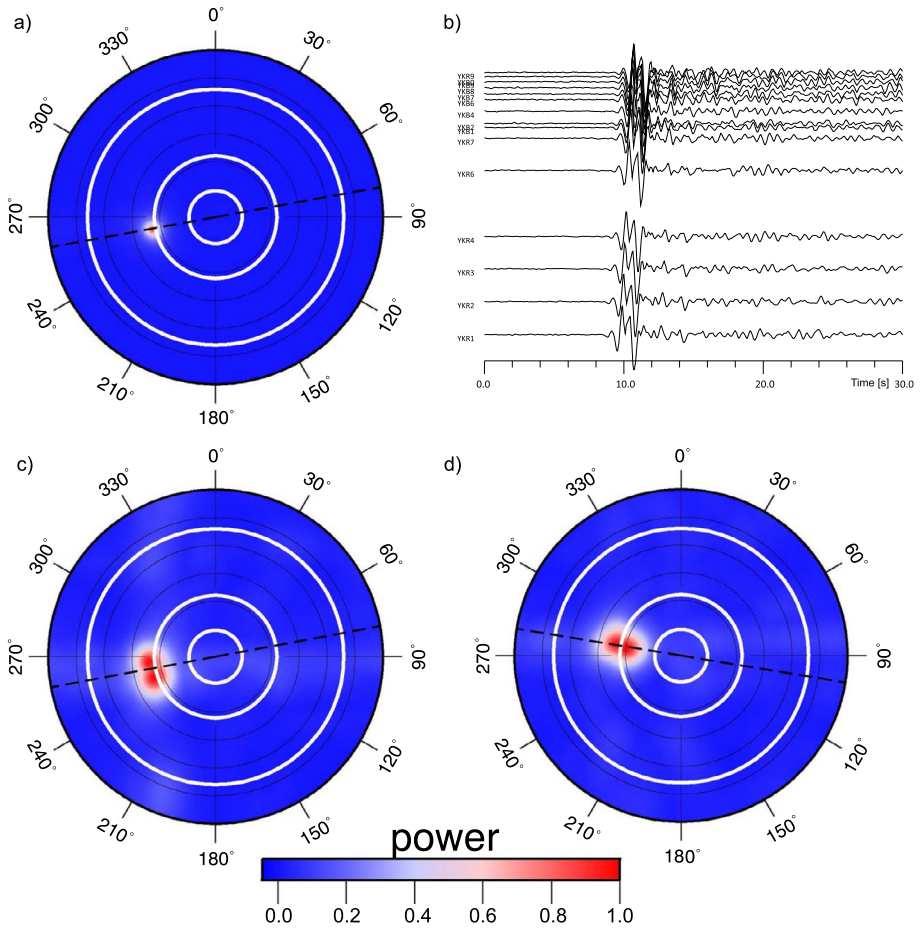

Fig. 3. Data examples. a) F-beampacking results for event on `03-JUN-2008_16:20` showing well focussed energy with little slowness vector uncertainty. b) Seismic traces for event shown in a) display by increasing epi-central distance. c) F-beampacking example of event `01-OCT-2002_08:46` showing multipathing. d) F-beampacking results for `09-SEP-2002_04:03` showing multipathing.

4. YKA mislocation vectors

YKA is a primary array of the International Monitoring System (IMS) to secure compliance with the Comprehensive Test Ban Treaty for nuclear tests. These stations are used for precise source location of earthquakes and potential underground nuclear explosions based on array processing. As such, the slowness and backazimuth deviations for IMS stations, in the form of mislocation vectors, are well studied (e.g. Bondár et al., 1999; Koch and Kradolfer, 1999). The measured slowness deviations for YKA are the smallest of the IMS primary arrays (Bondár et al., 1999; Koch and Kradolfer, 1999). The mislocation studies bin the differences between 1D expected and data determined slowness and backazimuth values in azimuth and slowness bins that are on the order of 10° for backazimuth and 2 s/° for slowness. Therefore, the reported slowness vector deviations for arrays will miss small-scale variation in slowness/backazimuth deviations as detected here.

The small average slowness vector deviations measured at YKA, that do not change considerably with incidence (Koch and Kradolfer, 1999; Bondár et al., 1999), are likely due to the simple and coherent crustal structure of the Slave craton underlying YKA. The smoothly varying mislocation vectors measured at YKA are often related to upper mantle structure as has been observed in other localities (Krüger and Weber, 1992; Schulte-Pelkum et al., 2003) indicating that the upper mantle beneath YKA is typically also not influencing the seismic wavefield much. As the slowness vector measurements integrate over the full path from source to receiver, source side structure might also influence our measurements. We could minimise the influence of near-source structure by analysing deep events only. This would reduce our dataset size and coverage considerably. We tested the effect of source side structure by restricting the analysis to events deeper than 300 km to reduce the potential impact of source side structure. We find that this leads to a similar distribution of the slowness vector deviations, indicating that source side structure likely is not a dominant factor to create the measured deviations reported here. We therefore attribute any strong slowness vector deviations observed to originate from deep Earth structure. Since the POLARIS stations were part of a temporary installation the slowness vector deviations for these stations have not been determined. Nonetheless, the stations are also located on the Slave craton with expected small lateral variations in structure. We therefore assume that slowness deviations due to near station structure are small.

5. Results

We calculate the *F*-beampacking for all events in the dataset. We observe that most *P*-wave events show well focused *F*-beampacks (Fig. 3a). Out of the more than 1000 *P*-wave events analysed we detect a small number ($\sim$ 5%) of events where the analysis cannot find a clear focus of the *F*-beampack, likely caused by very low signal-to-noise amplitude ratios. These events naturally show large errors in our error analysis and are excluded from further interpretation. We also detect evidence for multipathing in about 3% of the analysed events with no clear pattern emerging for the location of the turning points for the multipathed events (see Supp. Fig. 1). The backazimuth deviations in the multipathing events are on the order of a few degrees and are much

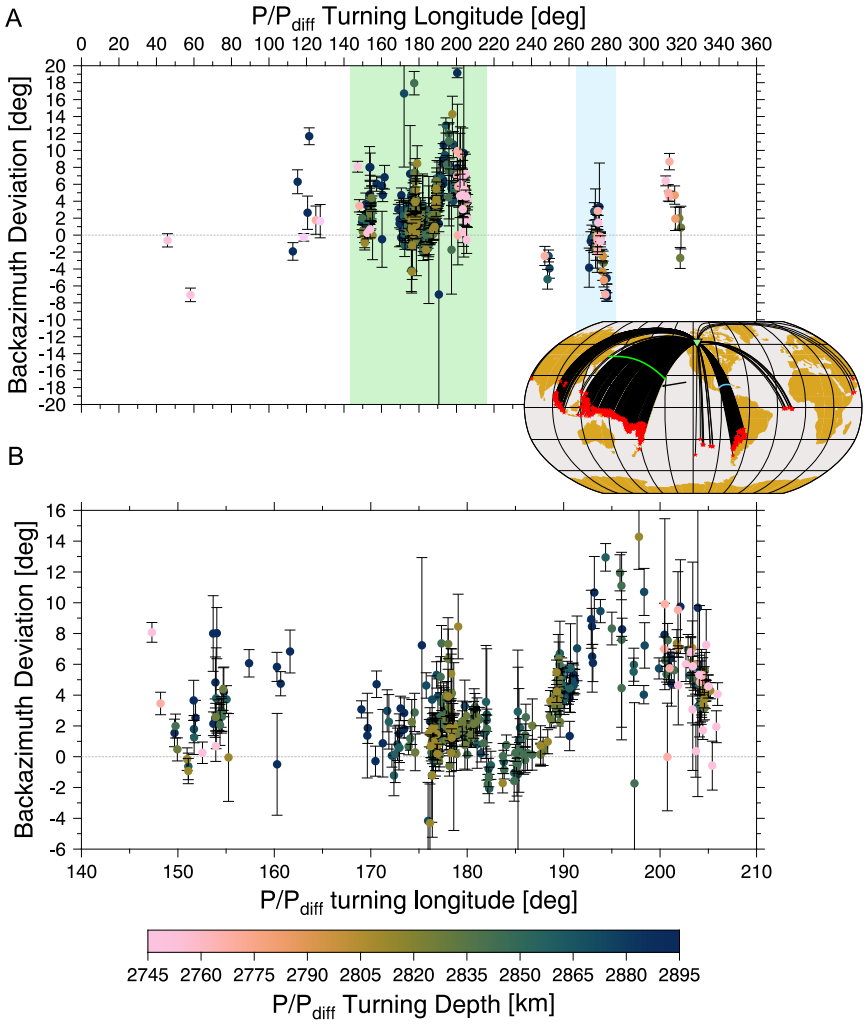

Fig. 4. Backazimuth deviations relative to the great circle path based on source and receiver location. Errors were determined through bootstrapping the original array traces. Only datapoints with errors less than 5 s/° are shown. A) Full dataset. Insert shows the ray paths of the dataset with the area of the most anomalous backazimuth measurements outlined by the yellow raypaths. Green profiles mark the areas highlighted in A. Arrow indicates the location of Hawaii. B) Focus on the densely sampled region of the Pacific. For the equivalent display of the *S*-wave results see Supplemental Figure 2.

smaller than the maximum deviations over the full dataset. Using the information from the slowness differences of the multipathed arrivals we can estimate the velocity differences between the two paths to be a maximum of 3 to 5%, well within the range of velocity variations expected in the lowermost mantle. Events with evidence for multipathing will likely result in larger uncertainties for the slowness vector in our bootstrapping approach but might indicate sharp velocity gradients close to the CMB (e.g. Ni et al., 2002; Ward et al., 2020).

Our best sampled region in the Pacific is characterized by strong, consistent *P*-wave backazimuth deviations of up to 14° relative to the great-circle path for events with bottoming or diffraction paths between E185° and E205°. The eastern edge of this anomaly is not well resolved due to a lack of sampling. Nonetheless, the backazimuth deviations (Fig. 4) return to the great-circle path at the end of the sampling area in the west, implying a return to undisturbed mantle velocities. We observe slowness variations in this area indicating a reduction in *P*-wave velocity (Fig. 5). A similar display with radial and transverse slowness residuals (relative to the theoretical IASP91 (Kennett and Engdahl, 1991) slowness and great circle path backazimuth) are provided as Supplemental Figure 4. The Pacific area sampled by the dataset shows a second area of strong and consistent deviations around E170° and E180° although the magnitude is smaller than between E185° and E205°. Deviations in this region are mainly clockwise, i.e. the energy arrives from a more westerly direction than expected from the great-circle path. Points sampling between E150° and E160° show mainly clockwise deviations although seem potentially less consistent. Further sampling in this area may map the precise nature of these deviations.

A further well-sampled region is located between E260° and E280° beneath central America and the Gulf of Mexico (Fig. 4) showing smaller deviations. In contrast to the Pacific backazimuth deviations, these show both clockwise and counterclockwise deviations on the order of ±(5° to 8°) with potentially a very sharp boundary around E270°. A small area is sampled in the northern Atlantic showing clockwise deviations of up to 8°.

Using the capabilities of YKA, we measure the full slowness vector also allowing us to map velocity variations based on the horizontal slowness (Fig. 5). We find velocity variation structure in general agreement with the larger scale structure resolved by tomography but also find stronger velocity variations than evident in tomography models. Fig. 5b shows the velocity variations relative to PREM (Dziewonski and Anderson, 1981) where we see evidence for the boundary of the LLVP in the transition from slow and fast velocities around E200°/N20°. We also detect a second boundary towards slow velocities beneath the Sea of Ochotsk and Sakhalin island boundary trending from E140°/N38° to E145°/N50° also in-

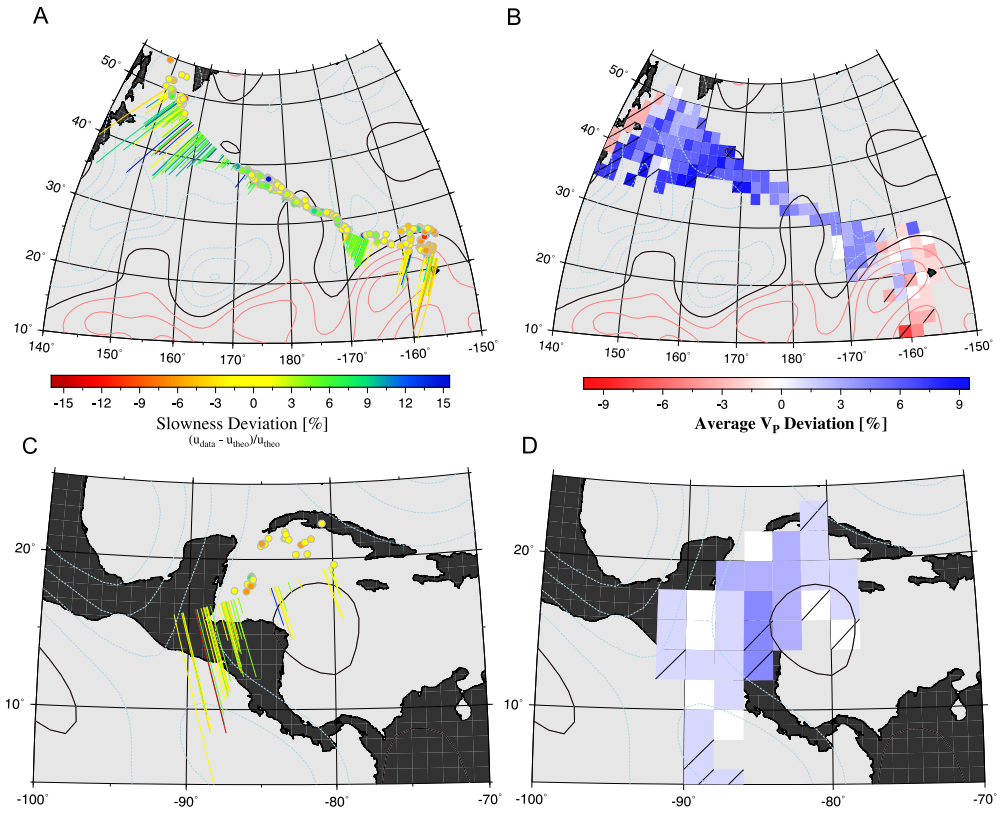

Fig. 5. Slowness deviations relative to 1D Earth model PREM Dziewonski and Anderson (1981). A) Full dataset with slowness deviation shown along the P_{diff} refraction path or at the bottoming point of the P path. Contour lines show the tomography model MIT-P08 Li et al. (2008) at the CMB given each ±0.25% with red lines being velocity reductions and blue increases. The 0% contour line is shown as solid line. Dashed line shows outline of area shown in B. B) Binned and averaged velocity deviations based on measured slowness values from dataset. The path length of the diffracted path is taken into account. Velocity changes are given relative to the CMB velocity of PREM. Bins with diagonal line are sampled by a single datapoint. The boundary of the LLVP seems to be visible in the south-east of the sampled region.

dicated in tomography models although this boundary is less well sampled.

We process the POLARIS *S*-wave data in the same way as the *P*-wave data. Due to the sparser dataset the continuous deviation is harder to identify (Supplemental Fig. 2). Qualitatively, the *S*-wave dataset shows a similar trend as the *P*-wave data. We find the strongest backazimuth deviations between E190° and E210° and beneath the Gulf of Mexico. Overall, we find slightly smaller deviations for *S*-waves with a non-zero mean which might indicate an influence of the background model. Due to the better sampling of the *P*-wave dataset we will focus on *P*-waves for the further discussion.

We analysed traveltime residuals of the P/P_{diff} arrivals relative to IASP91 (Kennett and Engdahl, 1991) theoretical times (see Suppl. Fig. 3A). Traveltimes residuals are within ± 4 s, with some of the longer P_{diff} waveforms being very emergent making precise picking difficult. We observe the strongest traveltime variance of the traveltime at the locations of the strongest backazimuth variance indicating a complex interaction of the wavefield with deep Earth structure. We have also analysed the traveltime deviations through our best-fitting velocity model (see Suppl. Fig. 3B). The traveltime residuals give comparable traveltime deviations to the data and there is qualitative agreement. We see the strongest deviations between data and model in the center region of the Aleutian anomaly which could indicate internal velocity structure that is not resolved by the backazimuth measurements.

Our results show that backazimuth deviations for individual events might be larger than previously reported (Ward et al., 2020) and might show coherent and consistent deviations from specific regions that can be used to sample the velocity structure of the Earth's interior.

6. Forward modeling

The backazimuth deviations in this dataset show a stronger signal than the observed slowness variations, likely sampling mantle structure along the path. Therefore we will focus on these in our modeling approach to derive a velocity model to explain the backazimuth deviations observed in this dataset. Slowness deviations (Fig. 5) have been used previously to map out e.g. lower mantle velocity variations (e.g. Xu and Koper, 2009) while similarly large backazimuth deviations for phases sampling the lowermost mantle are unusual. Since fully 3D wavefield propagation simulations at the required frequencies around 1 Hz are computationally very expensive, we adopt a 3D raytracing approach through 3D velocity models. We are using the 3D raytracing approach of Simmons et al. (2012) and perform grid searches over possible velocity deviations from a background model (Fig. 6). This approach uses layers representing finite thicknesses in the mantle, with velocity anomalies on a spherical tessellated grid.

The 3D raytracing provides us with synthetic traveltimes through our altered global velocity model from source to the individual array stations. To extract slowness vector information from these, we fit a plane to the variation of travel time as a function of latitude and longitude of each station in the array, which represents the moveout of the signal. Using the slope of this surface we decompose it into slowness and backazimuth. The backazimuth deviations are then defined as the predictions of the 3D versus the 1D models including the alteration to the 3D model as well the anomalies predicted along the path away from the CMB in the 3D background model. The model fit is calculated as the root mean square backazimuth deviation difference between the data and synthetics, for all modelled data points. We test different 3D

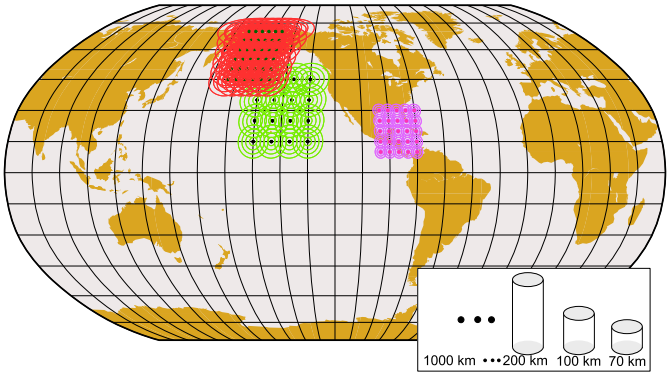

Fig. 6. Sampling grid for forward modeling. The three regions (Hawaii, Aleutians, Gulf of Mexico) are first modeled independently with combined and refined modeling in a second step. For each forward model grid point we model circular anomalies with varying diameters, velocity changes and heights above the CMB. See text for modeling details.

models of mantle velocity and attempt to minimise the misfit to the data.

Using this approach, multipathed events can potentially lead to inaccurate incidence angle measurement using the 3D raytracer. We indeed find evidence for multipathed arrivals in the traveltimes through our 3D velocity model although we do not observe a strong increase of multipathed arrivals between our background model and the best-fitting model. We avoid incorrect slowness vector measurements by introducing a misfit threshold of 0.1 s for the rms misfit when fitting a plane wavefront to the traveltimes to filter out events where multipathed arrivals arrive with strongly different traveltimes to the majority of the rays through the model. Inspecting all multipathed events we find that our chosen threshold is much smaller than the rms misfit for all multipathed events, so that we do not expect erroneous slowness vector results due to multipathed arrivals through the 3D model. We have not considered amplitude information for the raytraced arrivals with the possibility that the detected arrivals are too small to be observed in the dataset. More advanced wave propagation techniques might be necessary to verify the robustness of the raytracing results in the future.

We use subsets of the total dataset to reduce the computation time and allow testing of a greater number of velocity models. We seek to minimise the size of the dataset while retaining observations that provide sampling of independent paths, both in terms of latitude, longitude, and depth. Since we are using ray-theory in our modeling approach we are unable to model the P_{diff} paths of our dataset. To still cover the same area of the globe we have tested moving both source and receivers along the great circle path to a suitable distance where we first observe P arrivals. Changing the source and receiver configuration will change the paths through the 3D background velocity model slightly and therefore the slowness vector deviation contributions from the background model. We find that the changes are negligible compared to the deviations observed due to the altered velocity structure as only small changes to source and receiver locations are necessary and have moved the synthetic sources to avoid diffracted paths in our modeling.

The P_{diff} paths are sampling the structure at the CMB with P sampling above the CMB. Due to the restriction of the available sources we are limited to resolving structure to a maximum of about 400 km above the CMB with the sampling varying throughout the dataset due to the location of the seismicity.

We have tested a variety of 3D tomographic P-wave models as background models (Fig. 7a), including LLNL-G3Dv3 (Simmons et al., 2012), MIT-P08 (Li et al., 2008), GyPSuM (Simmons et al., 2010) and DETOX-P3 (Hosseini et al., 2020). Some of these models are able to explain the anomalies qualitatively, matching the general trend of deviations from certain directions (Fig. 7a). All models are unable to explain the magnitude of the deviations recorded in our data. This indicates that travel time anomalies exist in the region but the inversions are underpredicting the related velocity anomalies due to the inherent damping and regularization of the inversion process. We have also tested a recent full-waveform inversion tomography model (GLAD-M25, Lei et al. (2020)) that potentially resolves finer scale structure. We find that the differences compared to the traveltime tomography models in terms of backazimuth deviation are minor. We choose model MIT-P08 (Li et al., 2008) as the background model as it produces the lowest misfit between the recorded and synthetic backazimuth deviations for recent global P-wave models. We tested if an amplification of the velocity anomalies in the models can explain the measured anomalies. We found a moderately satisfactory fit to the data by increasing the velocity anomalies in the whole mantle by a factor of 3, but this lead to unreasonably large negative traveltime anomalies, thus we discount this model. A more plausible scenario in which velocities were increased by a factor of 3 only in the lowest 200 km of the mantle was also unable to fit the data.

To improve the fit between recorded and synthetic backazimuth deviations we introduce additional velocity heterogeneity into the 3D background model MIT-P08 (Li et al., 2008). We add velocity anomalies of greater magnitude than the background model, which shows extremes of only -1.2 and +0.8% *dVp* at the CMB across the whole Earth. We approximate anomalies as circular velocity reductions extending up from the CMB (Fig. 6). Within each anomaly we vary velocity change relative to the 3D reference model, radius, and centerpoint location in a grid search, as well as anomaly height above the CMB (i.e. thickness).

The circular shape is chosen for modelling simplicity and also because it represents the most parsimonious option in the absence of additional information on the shape of the anomalous velocity structure. In practical terms, the anomaly is as close as can be to circular when mapped onto the spherically tessellated grid, and so the modelled anomalies may not be truly circular. These anomalies overwrite the existing velocity structure within the background model. We separately model the two best sampled regions; beneath the mid-Pacific and Central America. For the Pacific we first simulate two separate anomalies to explain the two areas of strong backazimuth deviations (Fig. 4), which we term the Hawaiian and Aleutian anomalies. We vary the size and amplitude of these anomalies (independently of each other), with radii from 4° to 16° with a step size of 4° and velocity changes from -8% to -2% and a step size of 2% for the Hawaiian anomaly and -4% to -1% with a step size of 1% for the Aleutian anomaly. Anomaly locations are shifted in latitude and longitude by 10° and 5°, for the Hawaiian and Aleutian anomaly, respectively. For the Hawaiian anomaly, we test centre locations between N15° to N45° and E195° to E225° with step sizes of 10°. We test Aleutian anomaly center locations between N45° to N70° and E175° to E200° with step sizes of 5°. For the Hawaiian anomaly we initially test anomaly thicknesses (i.e. heights above the CMB) of 100, 200, 500, and 1000 km, and then repeat using a finer spacing for anomaly thickness of 30 km, 70 km, 100 km, 200 km, 300 km and 400 km. For the Aleutian anomaly we tested thicknesses of 30 km, 70 km, 100 km, 200 km, 300 km and 400 km.

Next, we construct models containing two anomalies in order to fit both Hawaiian and Aleutian anomalies simultaneously. Based on the misfit from the single anomaly models, we fix the location and properties of the Aleutian anomaly to N60°/W175°, with a radius of 12° and a velocity increase of 3% over the background model, and a thickness of 300 km. We then vary the Hawaiian anomaly location between N15° to N25° and E195° to E190° with 5° step size each. We test velocity variations from -8% to -2% with

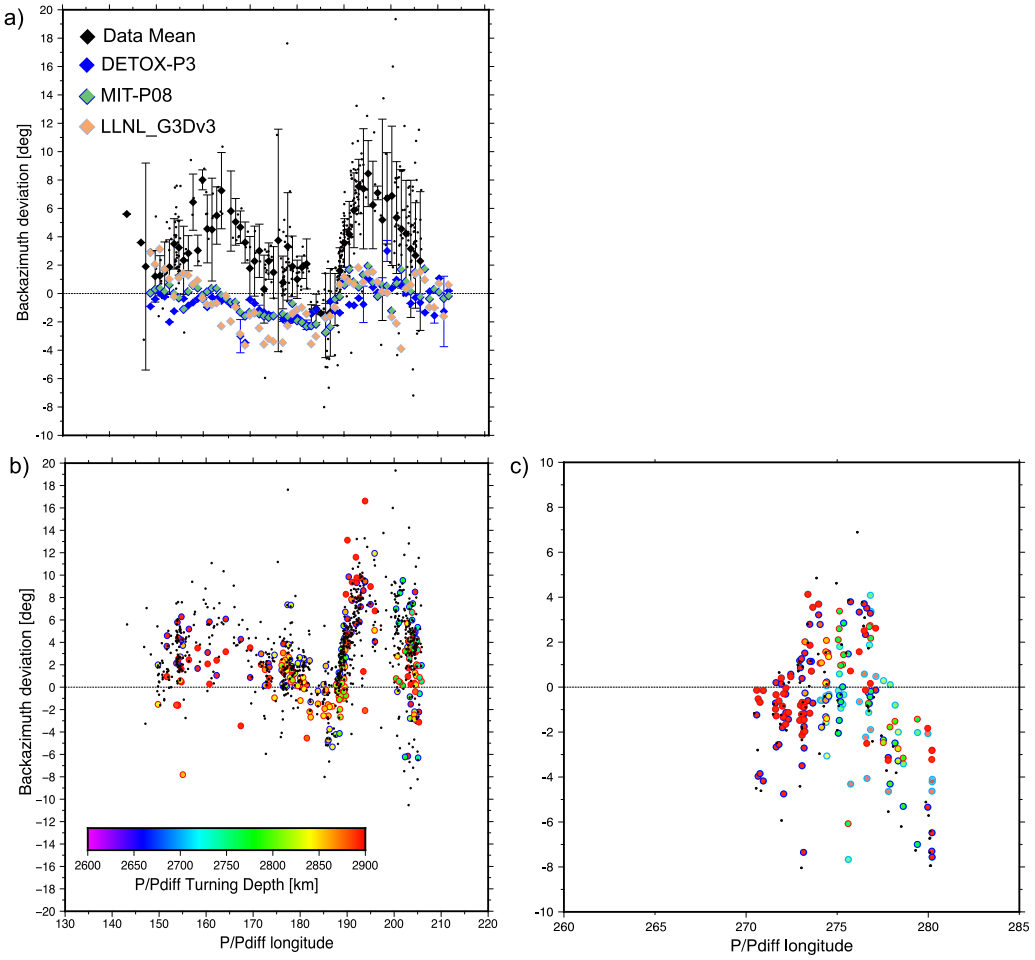

Fig. 7. Synthetic backazimuth deviations for different mantle velocity models. a) Comparison of backazimuth deviations from 3D tomographic velocity models for the synthetic dataset sampling the Pacific. Recorded backazimuth deviations are shown as black symbols with error bars. Symbol color indicates turning depths of the *P*-wave. b) Synthetic backazimuth deviations for the best fitting model for the Pacific region. Symbol color indicates turning depths of the *P*-wave. Recorded backazimuth deviations are shown as grey symbols. c) Synthetic backazimuth deviations for the best fitting model for the Gulf of Mexico. Recorded backazimuth deviations are shown as grey symbols. Symbol color indicates turning depths of the *P*-wave. Slow velocity model is indicated by symbols with black outlines and fast velocity model results are shown as symbols with thick blue outlines.

a step size of 2% and radii between 2° and 14° with 2° step size. For these models the thickness of the anomalies is chosen to be 70 km, 100 km and 200 km for the Hawaiian anomaly. In addition to the regular grid search, we refine the grids around local misfit minima to test further models.

In testing the Hawaiian anomaly, we find that the back-azimuth deviations at E185° - 195° and E200° - 205° longitude are difficult to fit with a single anomaly. As such, we perform a grid search for the location, thickness, width, and strength of two anomalies within this region. We search parameters of velocity variations from -2 to -8% relative to the background model with a step size of 1%, radii between 2-6° with a step size of 1°, latitudes between N20° and N30° with a 5° step size for both anomalies, and longitudes between W150° and W160°, and longitudes between W160° and W170° for the two anomalies. We then construct models containing the two anomalies in Hawaii and a third anomaly in the Aleutians.

In total, we have tested ∼4000 unique models for the Hawaiian anomaly, ∼5000 unique models for the Aleutian anomaly, and ∼800 unique models for the Central American anomaly.

We find that we can reproduce the observed backazimuth deviations well (Fig. 7) with the best-fitting velocity structures shown in Fig. 8 and Fig. 9 with the properties of the structures listed in Table 1. Anomaly location, strength, and height can be well constrained. Nonetheless, there are uncertainties in the data that can lead to several models fitting the data beneath the Gulf of Mexico almost equally well.

Table 1
Properties of the best fitting models for the two Hawaiian and Aleutian velocity anomalies. Two equally well-fitting structures for the Gulf of Mexico are listed. * denotes a minimum height due to the limited turning height of P/P_{diff} above the CMB.

Anomaly	Latitude [deg]	Longitude [deg]	Diameter [deg]	Height [km]	Velocity Anomaly [%]
Hawaii	N25	W155	2	200*	-8
Hawaii	N25	W165	6	70	-4
Aleutian	N60	W175	12	300*	+3
Gulf of Mexico A	N25	W85	2	200	-3
Gulf of Mexico B	N15	W75	4	200	+3

Using the forward modeling approach we find that a model with multiple additional velocity structures in addition to the 3D background velocity model is able to fit the data sampling the Pacific (Fig. 8). We find that two slow velocity structures in the vicinity of the surface location of the tip of the Hawaiian chain are able to explain the observed backazimuth deviations. These are located at N25°/W155° and N25°/W165° with diameters of 2° and 6°, respectively. Using the combination of *P* and P_{diff} paths in this area we are able to resolve the heights of these structures

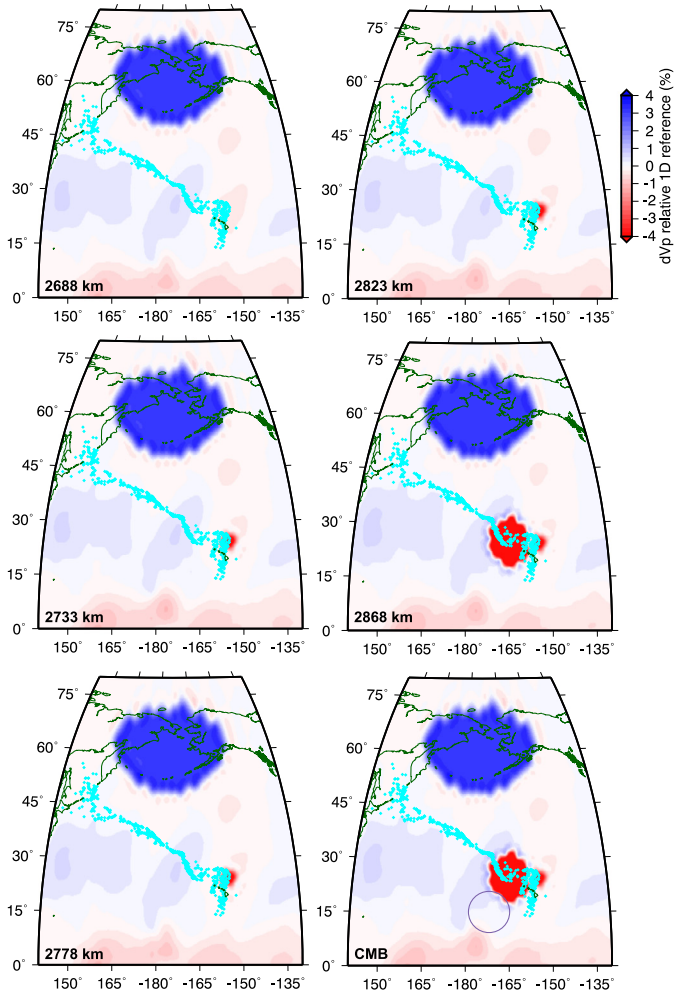

Fig. 8. Velocity structure of the best-fitting model for the Pacific. Shown is the velocity structure at depths of 2688 km, 2733 km, 2778 km, 2823 km, 2868 km and 2889 km (CMB) constrained by the spherical tesselation of LLNL-Earth3D (Simmons et al., 2012). Background model is MIT-P08 Li et al. (2008). Beneath Hawaii the broader western low velocity structure has a smaller height than the narrower eastern low velocity structure. Beneath the Aleutians we can track a high velocity structure throughout our sampled depth interval. We limit the modeling to circular structure (within the resolution of the model) and have not explored other geometries for the structures. Black circle indicates the approximated location of the 20 km thin ULVZ detected using S_{diff} postcursors (e.g. Cottaar and Romanowicz, 2012; Li et al., 2022) and the strongest ULVZ detected using ScS traveltimes (Jenkins et al., 2021) and *S*-waveforms (Kim et al., 2020). Due to the thin structure in this location the dataset analysed here is not sampling this region of the mantle.

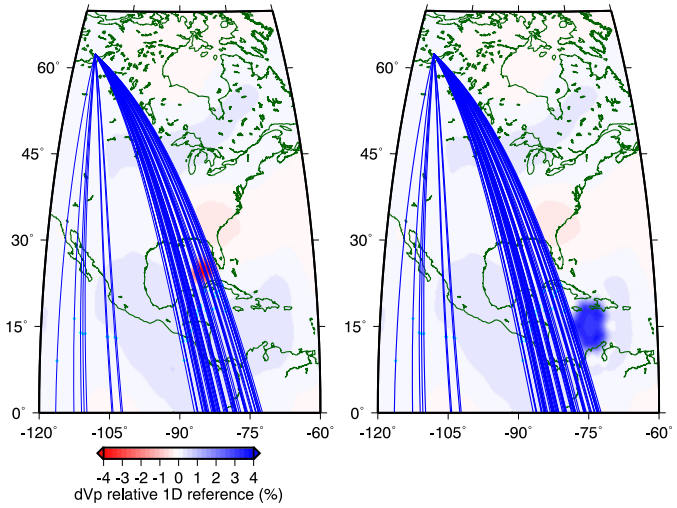

Fig. 9. a) Velocity structure of best fitting model including a low velocity anomaly with background velocity model MIT-P08 Li et al. (2008) beneath the Gulf of Mexico. b) Alternative model allowing similar fit to the data including a high-velocity anomaly beneath the Gulf of Mexico.

to be at least 200 km for the narrow eastern anomaly and 70 km for the wider western anomaly. We constrain the velocity reductions in these areas to be -4% for the western 200 km, and -8% for the eastern 70 km anomaly. To fit the furthest, eastern part of the profile in the Pacific we require a fast anomaly rising up to at least 300 km above the CMB with a diameter of 12° located at N60°/W175° showing a velocity increase of 3% to the 1D velocity background. This model is able to explain the backazimuth deviations of the dataset in the Pacific (Fig. 4).

The second well-sampled region is located beneath central America and the Gulf of Mexico (Fig. 4). We perform similar forward modeling to find the best fitting model to explain the observed backazimuth deviations. We modify location of slow and fast velocity anomalies ($-3 \leq dV_P \leq +3\%$) ranging from N10° to N30° latitude and E265° to E285° longitude in 5° increments. The velocity anomaly is modeled as circular with radii of 2° to 6° (in 2° increments) and with heights of 70, 100, 200 and 300 km. The background velocity model at the CMB in this region shows both fast velocities that are associated with the subduction and folding of the Cocos plate (Hutko et al., 2006), and some tomographic models also show slow velocities towards the east of the high-

velocity region, roughly located beneath Florida (e.g. Li et al., 2008; Lu et al., 2019; Hosseini et al., 2020).

We find that two models are able to explain our results equally well (Fig. 7, 9). We find either a 200 km tall, 3% velocity reduction with a diameter of 2° centred at N25°/W85° can fit the data, or else a 200 km tall structure located at N15°/W75° with a diameter of 4° and a velocity increase of 3% can explain the measured backazimuth deviation equally well.

7. Discussion

Our modeling demonstrates that the wavefield distortions that manifest as backazimuth deviations are able to resolve velocity structures along the raypaths and are most sensitive close to the turning point of the rays. The resolved velocity structures in the lowermost mantle are potentially stronger than those imaged by tomographic models and we can achieve higher resolution. Our background velocity model (MIT-P08) uses seismic traveltimes as data input for the inversion. Full-waveform inversion models are potentially able to resolve smaller scale structure and are able to resolve velocity anomalies more accurately. We tested a recent tomography models (GLAD-M25, Lei et al. (2020)) but find little advantage over MIT-P08 as background model. In this discussion we focus on the best sampled region in the central Pacific.

The central Pacific has previously been sampled using S_{diff} (Cottaar and Romanowicz, 2012; Li et al., 2022; To et al., 2011; Kim et al., 2020) indicating a thin (∼ 20 km), low velocity ($dV_S \approx$ -20%) ULVZ-type structure to the south west of the tip of the Hawaiian chain (centred around W172.3°/N15.4°). Different studies report different lateral extents for this anomaly up to 1000 km (Cottaar and Romanowicz, 2012). Similar structures have been resolved using *ScS* (Jenkins et al., 2021) resolving a larger scale ULVZ-type structure covering the CMB with a diameter of up to 1000 km with a thickness of ∼20 km. The structure and locations of these ULVZs are different from what we resolve using our dataset. We have tested the model proposed by Li et al. (2022) but it fails to explain our detected backazimuth anomalies likely due to the different datasets sampling the mantle differently with the dataset analysed here sampling higher above the CMB than 20 km in the vicinity of the Li et al. (2022) anomaly. Our *S*-wave dataset (Suppl. Fig. 2), although we do not model it in detail, shows comparable backazimuth deviations to the *P*-waves, indicating that we are sampling similar structures with both datasets and the difference between previous studies and the analysis here is likely not related to differences in *P* and *S*-wave structure. We conclude that due to the different source-receiver configuration between this and earlier studies we sample a different region of the lowermost mantle beneath the Pacific than earlier studies and cannot compare our resolved structure to the structures previously resolved. The detection of similar structures in close proximity might indicate a complex lower mantle in this region. The northern location of YKA leads to different sampling of the lowermost mantle in the Pacific. We therefore have no constraints on the structures reported earlier, but the additional detection of low velocity structures reported here indicates that a multitude of velocity anomalies might exist in the lowermost mantle and are not fully resolved by tomographic models.

Our best-fitting model for the Pacific consists of two slow anomalies relative to the background velocity model (MIT-P08 (Li et al., 2008)) close to the surface location of the Hawaiian intraplate volcanism (Fig. 10). We are able to track these structures to 70 km and at least 200 km above the CMB. The shorter (∼70 km), broader (∼8°) anomaly shows a velocity reduction (V_P) of ∼8% which is close to ULVZ properties, but the anomaly seems to be too tall for our current understanding of ULVZs (Yu and Garnero, 2018). The taller anomaly shows a velocity reduction of ∼4%,

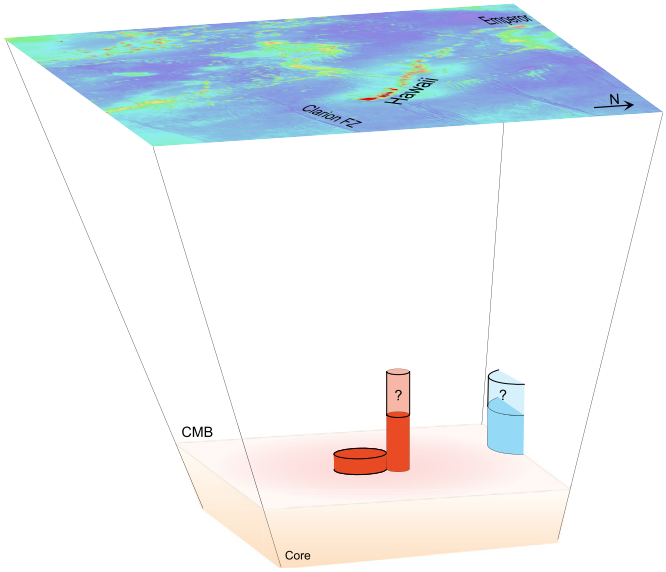

Fig. 10. Conceptual sketch of the Pacific structures resolved using P/P_{diff} backazimuth deviations. Red areas indicate velocity decreases mainly found beneath the Hawaiian Islands and blue structures indicate velocity increases found beneath the Aleutian subduction. The taller structure beneath Hawaii can be traced up to 200 km above the CMB, but might extend further towards the surface. Surface shows the topography and bathymetry of the region. Figure is not to scale.

which seems small for ULVZs. Its geometry (2° radius and at least 200 km height above the CMB) does not indicate ULVZ structure but indicates a narrow cylindrical structure rising from the CMB. The velocity reduction of 4% in the lowermost mantle could be explained by a thermal or thermo-chemical structure in a plume-like geometry (Goes et al., 2004; Ritsema et al., 2021).

We experiment with different boundary widths of the anomalies in our forward modeling through spatial smoothing. Still, we find that we require relatively sharp boundaries as indicated in our best fitting models to explain the sharp growth of the backazimuth deviations which support a thermo-chemical origin of the plume-like structures (Dannberg and Sobolev, 2015).

Due to the sampling of the anomalies our resolution of the width of the anomaly is better in south-east to north-west direction than in the along-ray direction. For ease of modeling, we model the anomalies as approximately circular features but have little constraint on the extent in south-west to north-east direction. Using crossing paths would help to reduce the uncertainties of the geometry.

The high velocity anomaly towards the Aleutians is likely related to the long standing subduction of slab material in this region likely forming a sheet-like fast structure in the mantle. We are not able to resolve this structure with the current modeling limitations. Due to the source-receiver configuration, which limits the turning point height above the CMB, we are not able to constrain the height of the top of the fast material and our simplified modeling is not able to resolve its detailed structure; our modeled anomaly is likely much larger in the along-ray direction than the true anomaly. Using *P*-waves recorded at shorter distances potentially can allow to track structures throughout the mantle. Nonetheless, we likely detect the effect of colder and faster subducted material on the seismic wavefield.

We find that two contrasting models for the paths crossing the Gulf of Mexico with both high and low velocity structure explain the backazimuth deviations similarly well. This indicates some non-uniqueness of the model which could be reduced by crossing paths and better sampling. Both structures seem reasonable for the region with the high velocity structure potentially related to the subduction of the Cocos plate (Hutko et al., 2006) and the

low velocity potentially related to partial melting at the edge of the slab (Thorne et al., 2019; Li, 2020). We also note the existence of a broader, weaker lower velocity areas in the tomography models (Fig. 9) in a similar location to the low velocity structure detected here.

8. Conclusions

We show that the directivity information, and especially the backazimuth, contains information on mantle velocity structure that can be used to map the Earth's interior. Using a dataset recorded at a small aperture array we are able to resolve small-scale low velocity structure in the central Pacific rising several 10 s to hundreds of kilometres away from the CMB showing velocity reductions of 4 to 8%. In the Pacific the location of two slow velocity anomalies is close to the tip of the Hawaiian volcanic chain potentially indicating a plume root at the CMB related to the intraplate volcanism at the surface. Our model indicates a broader base that then narrows to a thin roughly cylindrical structure. As such, this structure resembles plume structure as detected in recent tomographic models (e.g. French and Romanowicz, 2015) and could indicate a thermochemical plume root narrowing to a dominantly thermal, narrow upstream (Stockmann et al., 2019). Here, we are able to resolve sharp boundaries to this structure not resolved in recent tomographic models. We are also able to detect fast velocity structures with the backazimuth deviations that are in agreement with the subduction of the Pacific plate beneath the Aleutians and the Cocos plate beneath central America showing that fast and slow velocity anomalies can be resolved. Nonetheless, the dataset shown here shows some ambiguity of the results due to the dominant sampling direction for the dataset retrieved from a single array. This ambiguity of the derived velocity models could potentially be resolved with better sampling and crossing paths to better constrain velocity anomalies and structure. Using a combination of traveltimes and directivity information in joint inversions of seismic information might allow better resolution of the Earth's lowermost mantle.

CRediT authorship contribution statement

Sebastian Rost: Conceptualization, Formal analysis, Investigation, Methodology, Software, Visualization, Writing – original draft, Writing – review & editing. **Daniel A. Frost:** Formal analysis, Methodology, Software, Visualization, Writing – review & editing. **Andy Nowacki:** Methodology, Writing – review & editing. **Laura Cobden:** Methodology, Writing – review & editing.

Declaration of competing interest

The authors declare that they have no known competing financial interests or personal relationships that could have appeared to influence the work reported in this paper.

Data availability

All data is available from open data sources that have been referenced in the manuscript.

Acknowledgements

Sebastian Rost was partly supported by NERC grants 'NSFGEO-NERC: Global ultralow-velocity zone properties from seismic waveform modeling' (NE/R012199/1) and 'Structure and Composition of Large Low Shear Velocity Provinces' (NE/K006290/1). Daniel Frost was funded by the National Science Foundation grants 2050011, 2027181, and 2054964. Andy Nowacki was supported by a Leverhulme Early Career Fellowship and NERC grants 'REMIS: Reliable earthquake magnitudes for induced seismicity' (NE/R00154/1) and 'Mantle Circulation Constrained (MC^2): A multidisciplinary 4D Earth framework for understanding mantle upwellings' (NE/T012684/1). We thank editor Hanz Thybo for his editorial assistance and John Vidale and an anonymous reviewer for insightful reviews that helped to improve the manuscript.

Appendix A. Supplementary material

Supplementary material related to this article can be found online at https://doi.org/10.1016/j.epsl.2023.118011.

References

Blandford, R., 1974. An automatic event detector at the Tonto Forest seismic observatory. Geophysics 39, 633–643.
Bondár, I., North, R., Beall, G., 1999. Teleseismic slowness-azimuth station corrections for the international monitoring system seismic network. Bull. Seismol. Soc. Am. 89, 989–1003.
Cottaar, S., Romanowicz, B., 2012. An unsually large ULVZ at the base of the mantle near Hawaii. Earth Planet. Sci. Lett. 355–356, 213–222. https://doi.org/10.1016/j.epsl.2012.09.005.
Dannberg, J., Sobolev, S.V., 2015. Low-buoyancy thermochemical plumes resolve controversy of classical mantle plume concept. Nat. Commun. 6, 6960. https://doi.org/10.1038/ncomms7960.
Davies, D.R., Goes, S., Davies, J.H., Schuberth, B.S.A., Bunge, H.P., Ritsema, J., 2012. Reconciling dynamic and seismic models of Earth's lower mantle: the dominant role of thermal heterogeneity. Earth Planet. Sci. Lett. 353–354, 253–269. https://doi.org/10.1016/j.epsl.2012.08.016.
Dziewonski, A.M., Anderson, D.L., 1981. Preliminary reference Earth model. Phys. Earth Planet. Inter. 25, 297–356.
Efron, B., Tibshirani, R., 1986. Bootstrap methods for standard errors, confidence intervals, and other measures of statistical accuracy. Stat. Sci. 1, 54–77. https://doi.org/10.1214/ss/1177013815.
Ford, S., Garnero, E., McNamara, A., 2006. A strong lateral shear velocity gradient and anisotropy heterogeneity in the lowermost mantle beneath the southern Pacific. J. Geophys. Res. 111, B03306.
French, S.W., Romanowicz, B., 2015. Broad plumes rooted at the base of the Earth's mantle beneath major hotspots. Nature 525, 95–99. https://doi.org/10.1038/nature14876.
Frost, D.A., Rost, S., Garnero, E.J., Li, M., 2017. Seismic evidence for Earth's crusty deep mantle. Earth Planet. Sci. Lett. 470, 54–63. https://doi.org/10.1016/J.EPSL.2017.04.036.
Garnero, E., McNamara, A., 2008. Structure and dynamics of Earth's lower mantle. Science 626. https://doi.org/10.1126/science.1148028.
Goes, S., Cammarano, F., Hansen, U., 2004. Synthetic seismic signature of thermal mantle plumes. Earth Planet. Sci. Lett. 218, 403–419. https://doi.org/10.1016/S0012-821X(03)00680-0.
Hofmann, A., 1997. Mantle geochemistry: the message from oceanic volcanism. Nature 385, 219–229.
Hosseini, K., Sigloch, K., Tsekhmistrenko, M., Zaheri, A., Nissen-Meyer, T., Igel, H., 2020. Global mantle structure from multifrequency tomography using p, PP and p-diffracted waves. Geophys. J. Int. 220, 96–141. https://doi.org/10.1093/gji/ggz394.
Hutko, A., Lay, T., Garnero, E., Revenaugh, J., 2006. Seismic detection of folded, subducted lithosphere at the core-mantle boundary. Nature 441, 333–336.
Jellinek, A.M., Manga, M., 2002. The influence of a chemical boundary layer on the fixity, spacing and lifetime of mantle plumes. Solid State Phys. 418, 1–4. https://doi.org/10.1038/nature00898.1.
Jenkins, J., Mousavi, S., Li, Z., Cottaar, S., 2021. A high-resolution map of Hawaiian ULVZ morphology from ScS phases. Earth Planet. Sci. Lett. 563, 116885. https://doi.org/10.1016/j.epsl.2021.116885.
Kennett, B., Engdahl, E., 1991. Traveltimes for global earthquake location and phase identification. Geophys. J. Int. 105, 429–465.
Kim, D., Lekić, V., Ménard, B., Baron, D., Taghizadeh-Popp, M., 2020. Sequencing seismograms: a panoptic view of scattering in the core-mantle boundary region. Science 368, 1223–1228. https://doi.org/10.1126/science.aba8972.
Koch, K., Kradolfer, U., 1999. Determination of mislocation vectors to evaluate bias at GSETT-3 primary stations. J. Seismol. 3, 139–151. https://doi.org/10.1023/A:1009823825899.
Krüger, F., Weber, M., 1992. The effect of low-velocity sediments on the mislocation vectors of the GRF array. Geophys. J. Int. 108, 387–393. https://doi.org/10.1111/j.1365-246X.1992.tb00866.x.
Lei, W., Ruan, Y., Bozdağ, E., Peter, D., Lefebvre, M., Komatitsch, D., Tromp, J., Hill, J., Podhorszki, N., Pugmire, D., 2020. Global adjoint tomography—model GLAD-M25. Geophys. J. Int. 223, 1–21. https://doi.org/10.1093/GJI/GGAA253.

Lekic, V., Cottaar, S., Dziewonski, A., Romanowicz, B., 2012. Cluster analysis of global lower mantle tomography: a new class of structure and implications for chemical heterogeneity. Earth Planet. Sci. Lett. 357–358, 68–77. https://doi.org/10.1016/j.epsl.2012.09.014.

Li, C., van der Hilst, R.D., Engdahl, E.R., Burdick, S., 2008. A new global model for P-wave speed variations in Earth's mantle. Geochem. Geophys. Geosyst. 9. https://doi.org/10.1029/2007GC001806.

Li, M., 2020. The formation of hot thermal anomalies in cold subduction-influenced regions of Earth's lowermost mantle. J. Geophys. Res., Solid Earth 125, e2019JB019312. https://doi.org/10.1029/2019JB019312.

Li, Z., Leng, K., Jenkins, J., Cottaar, S., 2022. Kilometer-scale structure on the core–mantle boundary near Hawaii. Nat. Commun. 13, 1–8. https://doi.org/10.1038/s41467-022-30502-5.

Lu, C., Grand, S.P., Lai, H., Garnero, E.J., 2019. TX2019slab: a new p and s tomography model incorporating subducting slabs. J. Geophys. Res., Solid Earth 124, 11549–11567. https://doi.org/10.1029/2019JB017448.

McNamara, A., Zhong, S., 2005. Thermochemical structures beneath Africa and the Pacific Ocean. Nature 437, 1136–1139.

Morgan, W., 1971. Convection plumes in the lower mantle. Nature 230, 42–43.

Natural Resources Canada (NRCAN Canada), 1975. Canadian national seismograph network [data set]. http://www.fdsn.org/doi/10.7914/SN/CN. https://doi.org/10.7914/SN/CN.

Ni, S., Tan, E., Gurnis, M., Helmberger, D., 2002. Sharp sides to the African superplume. Science 296, 1850–1852. https://doi.org/10.1126/science.1070698.

Ritsema, J., Deuss, A., van Heijst, H.J., Woodhouse, J.H., 2011. S40RTS: a degree-40 shear-velocity model for the mantle from new Rayleigh wave dispersion, teleseismic traveltime and normal-mode splitting function measurements. Geophys. J. Int. 184, 1223–1236. https://doi.org/10.1111/j.1365-246X.2010.04884.x.

Ritsema, J., Maguire, R., Cobden, L., Goes, S., 2021. Seismic imaging of deep mantle plumes. In: Mantle Convection and Surface Expressions, pp. 353–369.

Schulte-Pelkum, V., Vernon, F.L., Eakins, J., 2003. Large teleseismic P wavefront deflections observed with broadband arrays. Bull. Seismol. Soc. Am. 93, 747–756. https://doi.org/10.1785/0120020126.

Selby, N.D., 2008. Application of a generalized F detector at a seismometer array. Bull. Seismol. Soc. Am. 98, 2469–2481. https://doi.org/10.1785/0120070282.

Shephard, G.E., Matthews, K.J., Hosseini, K., Domeier, M., 2017. On the consistency of seismically imaged lower mantle slabs. Sci. Rep. 7, 10976. https://doi.org/10.1038/s41598-017-11039-w.

Simmons, N., Myers, S., Johannesson, G., Matzel, E., 2012. LLNL-G3Dv3: global P wave tomography model for improved regional and teleseismic travel time prediction. J. Geophys. Res. 117, B10302. https://doi.org/10.1029/2012JB009525.

Simmons, N.A., Forte, A.M., Boschi, L., Grand, S.P., 2010. GyPSuM: a joint tomographic model of mantle density and seismic wave speeds. J. Geophys. Res. 115, 1–24. https://doi.org/10.1029/2010JB007631.

Stockmann, F., Cobden, L., Deschamps, F., Fichtner, A., Thomas, C., 2019. Investigating the seismic structure and visibility of dynamic plume models with seismic array methods. Geophys. J. Int. 219, S167–S194. https://doi.org/10.1093/GJI/GGZ334.

Thorne, M.S., Takeuchi, N., Shiomi, K., 2019. Melting at the edge of a slab in the deepest mantle. Geophys. Res. Lett. 46, 2019GL082493. https://doi.org/10.1029/2019GL082493.

To, A., Fukao, Y., Tsuboi, S., 2011. Evidence for a thick and localized ultra low shear velocity zone at the base of the mantle beneath the central Pacific. Phys. Earth Planet. Inter. 184, 119–133. https://doi.org/10.1016/j.pepi.2010.10.015.

To, A., Romanowicz, B., Capdeville, Y., Takeuchi, N., 2005. 3D effects of sharp boundaries at the borders of the African and Pacific superplumes: observation and modeling. Earth Planet. Sci. Lett. 233, 137–153. https://doi.org/10.1016/j.epsl.2005.01.037.

Ward, J., Nowacki, A., Rost, S., 2020. Lateral velocity gradients in the African lower mantle inferred from slowness-space observations of multipathing. Geochem. Geophys. Geosyst. https://doi.org/10.1029/2020GC009025.

Xu, Y., Koper, K.D., 2009. Detection of a ULVZ at the base of the mantle beneath the northwest Pacific. Geophys. Res. Lett. 36. https://doi.org/10.1029/2009GL039387.

Yu, S., Garnero, E.J., 2018. Ultralow velocity zone locations: a global assessment. Geochem. Geophys. Geosyst. 19, 396–414. https://doi.org/10.1002/2017GC007281.

Zhong, S., 2006. Constraints on thermochemical convection of the mantle from plume heat flux, plume excess temperature, and upper mantle temperature. J. Geophys. Res., Solid Earth 111. https://doi.org/10.1029/2005JB003972.